

Neutron-rich isotope production for $Z \geq 98$ in $^{238}\text{U} + ^{248}\text{Cm}$ reaction

S.E. Ocal,¹ O. Yilmaz,¹ S. Ayik,^{2,*} and A. S. Umar³

¹Physics Department, Middle East Technical University, 06800 Ankara, Turkey

²Physics Department, Tennessee Technological University, Cookeville, TN 38505, USA

³Department of Physics and Astronomy, Vanderbilt University, Nashville, TN 37235, USA

(Dated: November 19, 2024)

Background: Multi-nucleon transfer (MNT) reactions in actinide systems are a promising method to synthesize transuranium neutron-rich elements. Appropriate theoretical approaches are needed to understand the mechanism behind MNT.

Purpose: This work aims to produce neutron-rich isotopes in the super-heavy region through the $^{238}\text{U} + ^{248}\text{Cm}$ system. We employ a microscopic approach to elucidate reaction mechanisms, and predict new isotope production that expands the known nuclear chart.

Methods: The stochastic mean-field (SMF) approach, including fluctuations and correlations, is used to explain the primary cross-sections in MNT reactions based on the quasi-fission and inverse quasi-fission processes, and a statistical de-excitation model with GEMINI++ code to calculate the secondary fragment cross-sections.

Results: The calculated cross-sections using SMF and GEMINI++ explain available experimental results for the $^{238}\text{U} + ^{248}\text{Cm}$ system at $E_{\text{c.m.}} = 898.7$ MeV energy. This shows the effectiveness and applicability of the quantal diffusion approach based on the SMF theory in heavy-ion collisions.

Conclusions: Production of transuranium neutron-rich elements with a proton number up to $Z=101$ are obtained with sizable cross-sections. Theoretical results calculated for the $Z=102-105$ region, for which there are no experimental data, show that the cross-section values would be lower than the microbarn level. SMF theory does not contain any adjustable parameters other than the standard parameters of the energy density functional used in the TDHF theory and is an important approach for the microscopic understanding of reaction mechanisms.

I. INTRODUCTION

Extensive theoretical and experimental research is underway to produce heavy elements in the region between the presently known isotopes and the driplines, particularly in the upper half of the nuclear chart on the neutron-rich side. Production of the unknown isotopes closed to the neutron and proton drip lines will give new input for the models, particularly new spherical and deformed shell effects in the region of super-heavy nuclei. Fusion is presently the only method to synthesize transuranium and superheavy nuclei, but the measured production cross-sections are expected to be very small, below picobarns, requiring an increase in beam intensities and improvement in experimental techniques for isotope separation and detection [1,2]. Multi-nucleon transfer (MNT) reactions that occur in deep-inelastic binary collisions near the Coulomb barrier energies are an alternate method for producing neutron-rich heavy isotopes using actinide targets, and is being experimentally studied in laboratories around the world [3].

Theoretically, several phenomenological techniques, such as the multidimensional Langevin model [4–9], the di-nuclear system model [10,11], and the quantum molecular dynamics model [12–14] have been used to study the multinucleon transfer mechanism. The time-dependent Hartree-Fock (TDHF) theory provides a microscopic description of reaction dynamics and has been widely used to analyze MNT reactions [15–25]. Beyond the mean-field approximation

of TDHF, the time-dependent random phase approximation (TDRPA), developed by Balian and Vénéroni, is used for symmetric systems [26–31]. The stochastic mean-field (SMF) approach, which includes mean-field fluctuations and correlations between proton and neutron transfers, provides an additional improvement to the TDHF theory, where quantal effects, memory effects, and the full collision geometry are included [32,33]. In the SMF framework, the production cross sections of neutron-rich isotopes based on quasi-fission reactions (QF) and inverse quasi-fission reactions (IQF) in MNT reactions can be calculated [34–42]. This work presents our theoretical results for MNT reactions of the $^{238}\text{U} + ^{248}\text{Cm}$ system at $E_{\text{c.m.}} = 898.7$ MeV energy by employing the SMF approach to synthesize neutron-rich nuclei above $Z \geq 98$. Here, $^{238}\text{U} + ^{248}\text{Cm}$ is preferred as one of the heaviest and most neutron-rich available target materials. In addition, the excited primary products are cooled down using the statistical de-excitation GEMINI++ code and the production cross-sections for the secondary fragments are calculated. The $^{238}\text{U} + ^{248}\text{Cm}$ system at $E_{\text{c.m.}} = 898.7$ MeV energy has been studied both experimentally [43–45] and theoretically [4,46,47]. In this work, the production cross sections of the primary and secondary products in the transuranium region (such as Cf, Es, Fm, Md) are calculated by choosing four different initial orientations of projectile and target nuclei and compared with experimental data. We also present the calculation for $Z = 102-105$ (No, Lr, Rf, and Db) for which there are no experimental data. We briefly discuss the theoretical framework of the cross-section calculations for reaction products in Sec. II. In Sec. III, we present our calculations for the $^{238}\text{U} + ^{248}\text{Cm}$ system at $E_{\text{c.m.}} = 898.7$ MeV energy using the quantal transport description based on the SMF approach. Conclusions are

* ayik@tntech.edu

presented in Sec. IV.

II. THEORETICAL FRAMEWORK

A. Primary cross-sections of reaction products

In quasifission reactions, the colliding ions stick and move together for an extended time compared to typical reaction times, during this time they exchange nucleons without fusing, they then separate into the primary di-nuclear system with different numbers of neutrons and protons than the initial ones. We calculate the cross-sections for the production of primary isotopes using the standard expression,

$$\sigma^{pri}(N, Z) = \frac{\pi \hbar^2}{2\mu E_{c.m.}} \sum_{\ell_{min}}^{\ell_{max}} (2\ell + 1) \frac{1}{2} [P_{\ell}^{pro}(N, Z) + P_{\ell}^{tar}(N, Z)] \quad (1)$$

In this expression, $P_{\ell}^{pro}(N, Z)$ and $P_{\ell}^{tar}(N, Z)$ denote the normalized probability distribution of producing projectile-like and target-like fragments. The factor of 1/2 is introduced to normalize the total distribution of the primary fragment to unity. A Fokker-Planck type equation [48] describes the evolution of the probability distribution function of macroscopic variables, which is a correlated Gaussian function of the mean values of neutron, proton, and mixed dispersions

$$P_{\ell}(N, Z, t) = \frac{1}{2\pi\sigma_{NN}(\ell)\sigma_{ZZ}(\ell)\sqrt{1-\rho_{\ell}^2}} \exp(-C_{\ell}). \quad (2)$$

Here, the exponent C_{ℓ} for each initial angular momentum is given by

$$C_{\ell} = \frac{1}{2(1-\rho_{\ell}^2)} \left[\left(\frac{Z-Z_{\ell}}{\sigma_{ZZ}(\ell)} \right)^2 - 2\rho_{\ell} \left(\frac{Z-Z_{\ell}}{\sigma_{ZZ}(\ell)} \right) \left(\frac{N-N_{\ell}}{\sigma_{NN}(\ell)} \right) + \left(\frac{N-N_{\ell}}{\sigma_{NN}(\ell)} \right)^2 \right], \quad (3)$$

with the correlation coefficient $\rho_{\ell} = \sigma_{NZ}^2(\ell)/\sigma_{ZZ}(\ell)\sigma_{NN}(\ell)$. Quantities N_{ℓ} and Z_{ℓ} denote the mean neutron and proton numbers of the target-like and projectile-like fragments that are determined by the TDHF calculations. Dispersions satisfy a set of coupled differential equations [49,50]

$$\frac{\partial}{\partial t} \sigma_{NN}^2 = 2 \frac{\partial v_n}{\partial N_1} \sigma_{NN}^2 + 2 \frac{\partial v_n}{\partial Z_1} \sigma_{NZ}^2 + 2D_{NN}, \quad (4)$$

$$\frac{\partial}{\partial t} \sigma_{ZZ}^2 = 2 \frac{\partial v_p}{\partial Z_1} \sigma_{ZZ}^2 + 2 \frac{\partial v_p}{\partial N_1} \sigma_{NZ}^2 + 2D_{ZZ}, \quad (5)$$

$$\frac{\partial}{\partial t} \sigma_{NZ}^2 = \frac{\partial v_p}{\partial N_1} \sigma_{NN}^2 + \frac{\partial v_n}{\partial Z_1} \sigma_{ZZ}^2 + \sigma_{NZ}^2 \left(\frac{\partial v_p}{\partial Z_1} + \frac{\partial v_n}{\partial N_1} \right) \quad (6)$$

To determine neutron, proton, and mixed dispersions we need to calculate the diffusion coefficients (D_{NN} and D_{ZZ}) of neutrons and protons, and the derivatives of the drift coefficients ($v_p(t)$ and $v_n(t)$).

B. Quantal diffusion coefficients

In the nucleon diffusion mechanism, the neutron number and proton number of the projectile-like or target-like fragments are the relevant macroscopic variables. For each stochastically generated event λ in an ensemble, the neutron and proton numbers, $N_1^{\lambda}(t)$ and $Z_1^{\lambda}(t)$, are determined by integrating the nucleon density over the projectile side of the window between the colliding nuclei. Based on SMF theory, the rate of changes of neutron and proton numbers $dN_1(t)/dt$ and $dZ_1(t)/dt$ satisfy a coupled set of Langevin equations. We consider the small amplitude fluctuations and linearize the Langevin equation around the mean values of the macroscopic variables $N_1^{\lambda}(t) = N_1(t) - \delta N_1^{\lambda}(t)$ and $Z_1^{\lambda}(t) = Z_1(t) - \delta Z_1^{\lambda}(t)$. The mean values $N_1(t)$ and $Z_1(t)$ are determined by the mean-field description of TDHF theory for small amplitude fluctuations. The fluctuations of the neutron and proton numbers δN_1^{λ} , δZ_1^{λ} evolve according to coupled linear quantal Langevin equations [48–53],

$$\frac{d}{dt} \begin{pmatrix} \delta Z_1^{\lambda} \\ \delta N_1^{\lambda} \end{pmatrix} = \begin{pmatrix} \frac{\partial v_p}{\partial Z_1} (Z_1^{\lambda} - \bar{Z}_1) + \frac{\partial v_p}{\partial N_1} (N_1^{\lambda} - \bar{N}_1) \\ \frac{\partial v_n}{\partial Z_1} (Z_1^{\lambda} - \bar{Z}_1) + \frac{\partial v_n}{\partial N_1} (N_1^{\lambda} - \bar{N}_1) \end{pmatrix} + \begin{pmatrix} \delta v_p^{\lambda}(t) \\ \delta v_n^{\lambda}(t) \end{pmatrix}. \quad (7)$$

Langevin equation is equivalent to the Fokker-Plank equation for the distribution function of the macroscopic variables. The stochastic part of the drift coefficients $\delta v_{n,p}^{\lambda}(t)$, which provides the source for generating fluctuations in mass and charge asymmetry degrees of freedom, are determined by uncorrelated Gaussian distributions with zero mean values $\overline{\delta v_{n,p}^{\lambda}(t)} = 0$. The integration of these autocorrelation functions over history defines the diffusion coefficients $D_{NN}(t)$ for proton and neutron transfers [51,52]

$$\int_0^t dt' \overline{\delta v_{\alpha}^{\lambda}(t) \delta v_{\alpha}^{\lambda}(t')} = D_{\alpha\alpha}(t). \quad (8)$$

Diffusion coefficients generally involve a complete set of particle-hole states [34]. It is possible to eliminate the entire set of particle states by employing closure relations in a diabatic limit [53]. This results in an important simplification, and as a result, diffusion coefficients are determined entirely in terms of the occupied single-particle wave functions of TDHF evolution. Explicit expressions of diffusion coefficients are provided in previous publications [34–36]. The fact that diffusion coefficients are determined by the mean-field properties is consistent with the fluctuation-dissipation theorem of non-equilibrium statistical mechanics and it greatly simplifies calculations of quantal diffusion coefficients. Diffusion coefficients include the quantal effects due to shell structure, Pauli blocking, and the full effect of the collision's geometry without any adjustable parameters. The direct part is

given as the sum of the nucleon currents across the window from the target-like fragment to the projectile-like fragment and from the projectile-like fragment to the target-like fragment, which is integrated over the memory. This is analogous to the random walk problem, in which the diffusion coefficient is given by the sum of the rate for forward and backward steps [52–54]. The second part in the quantal diffusion expression stands for the Pauli blocking effects in the nucleon transfer mechanism, which does not have a classical counterpart [34],

$$\begin{aligned}
D_{\alpha\alpha}(t) = & \int_0^t d\tau \int d^3r g(x') \left[G_T(\tau) J_{\perp\alpha}^T(\vec{r}, t - \frac{\tau}{2}) \right. \\
& + G_P(\tau) J_{\perp\alpha}^P(\vec{r}, t - \frac{\tau}{2}) \left. \right] \\
& - \int_0^t d\tau \text{Re} \left[\sum_{h' \in P, h \in T} A_{h'h}^\alpha(t) A_{h'h}^{\alpha*}(t - \tau) \right. \\
& + \left. \sum_{h' \in T, h \in P} A_{h'h}^\alpha(t) A_{h'h}^{\alpha*}(t - \tau) \right]. \quad (9)
\end{aligned}$$

Detailed derivation and the definition of the terms in Eq. (9) can be seen in Ref. [34].

C. Derivatives of drift coefficients

Derivatives of neutron and proton drift coefficients with respect to neutron and proton numbers cannot be obtained directly from the TDHF calculations. The proton and neutron drift in the $N - Z$ plane is determined by the potential energy surface of the di-nuclear system. As a result of the symmetry energy, drift occurs rapidly in the direction perpendicular to the mean drift path (the beta stability valley), causing rapid equilibration of the charge asymmetry, and drift continues slowly along the beta stability valley [50,55]. However, when the charge asymmetries of the colliding ions are very close, rapid equilibration of the charge asymmetry does not occur. For this case, a neighboring system under the same initial conditions could be used for a drift toward the stability valley. The potential energy surface dominates the nuclear transfers and is given in two parabolic forms for a di-nuclear system,

$$U(N_1, Z_1) = \frac{1}{2} a R_S^2(N_1, Z_1) + \frac{1}{2} b R_V^2(N_1, Z_1). \quad (10)$$

Here, $R_S(N_1, Z_1)$ and $R_V(N_1, Z_1)$ represent the perpendicular distances of a fragment with neutron and proton numbers (N_1, Z_1) from the isoscalar path and the local equilibrium state along the isoscalar path, respectively. Because of the sharp increase of asymmetry energy, we expect the isovector curvature parameter a to be much larger than the isoscalar curvature parameter b . Drift coefficients in the over-damped limit are linked to the potential energy surface in the $(N - Z)$ -plane in terms of Einstein relations as follows [50,54,55]

$$v_n(t) = -\frac{D_{NN}(t)}{T^*} \frac{\partial}{\partial N_1} U(N_1, Z_1) \quad (11a)$$

$$v_z(t) = -\frac{D_{ZZ}(t)}{T^*} \frac{\partial}{\partial Z_1} U(N_1, Z_1), \quad (11b)$$

where T^* represents the effective temperature of the system. By using Einstein relations, the reduced curvature parameters $\alpha = a/T^*$ and $\beta = b/T^*$ are estimated in terms of drift and diffusion coefficients. As a result of shell effects and microscopic collision dynamics in the TDHF description, reduced curvature parameters depend on time. In the macroscopic transport description, we estimate reduced curvature parameters by carrying out an averaging over a suitable time interval.

D. Secondary cross-sections of reaction products

The primary fragments produced in the heavy-ion collisions cool down through three main mechanisms: the emission of light particles, fission or isotope decay, and gamma radiation. We use a statistical GEMINI++ code for the de-excitation mechanisms of these primary fragments [56]. The GEMINI++ code uses the Hauser Feshbach formalism [57] for the light particle evaporation process, the Bohr-Wheeler formalism [58], and the Moretto formalism [59] for mass symmetric and asymmetric fission decays, and finally the approach of Blatt and Weisskopf [60] for gamma radiation. The total excitation energy of a reaction channel is found from the expression $E_{tot}^* = E_{c.m.} - TKE(\ell) + Q(N, Z)$. Here, the total kinetic energy (TKE) and Q -value of the reaction channel for each initial angular momentum are calculated within TDHF. The total excitation energy and the orbital angular momentum are distributed to the reaction products in proportion to their masses. The statistical code GEMINI++ calculates the probability $W_\ell(N, Z \rightarrow N', Z')$ of reaching the final nucleus (N', Z') starting from an excited parent nucleus with the number of neutrons and protons (N, Z) and the excitation energy $E_\ell^*(N, Z)$ that decays by a series of consecutive binary decays until it becomes energetically forbidden. Then the probability distribution of secondary isotopes can be expressed as

$$P_\ell^{sec}(N', Z') = \sum_{N \geq N'} \sum_{Z \geq Z'} (2\ell + 1) P_\ell^{pri}(N, Z) W_\ell(N, Z \rightarrow N', Z'), \quad (12)$$

The total secondary isotope production cross-section covering all projectile-like (PLF) and target-like (TLF) product pairs of the binary nuclear system according to the probability distributions is as follows:

$$\sigma^{sec}(N', Z') = \frac{\pi \hbar^2}{2\mu E_{c.m.}} \sum_{\ell_{\min}}^{\ell_{\max}} (2\ell + 1) P_\ell^{sec}(N', Z'). \quad (13)$$

III. RESULTS AND DISCUSSIONS

The mean-field theory describes the one-body dissipation process and the most likely dynamical path of the collective

motion for low-energy heavy-ion collisions. The TDHF theory is a deterministic approach for many body dynamics since mean-field development from a given initial condition to a single final state is a deterministic process. In $^{238}\text{U} + ^{248}\text{Cm}$, both projectile and target nuclei exhibit strong prolate deformation in their ground states, and therefore collision dynamics and MNT mechanism strongly depend on the collision geometry. We examine four different initial collision configurations at the same energy $E_{c.m.} = 898.7$ MeV shown in Fig. 1. We use the letters X and Y to represent the target's or projectile's initial orientation, respectively, perpendicular to and along the beam direction, in analogy with the work of Kedziora and Simenel of [61]. The symbols XX, XY, YX, and YY stand for four distinct collision geometries, which correspond to tip-tip, tip-side, side-tip, and side-side geometries, in that order. The

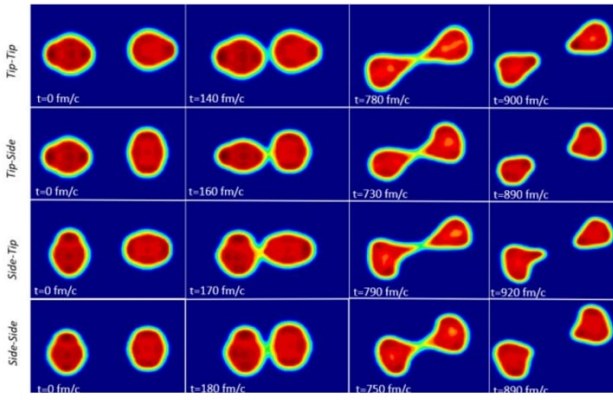


FIG. 1. Snapshots of density profiles in the collisions of $^{238}\text{U} + ^{248}\text{Cm}$ $E_{c.m.} = 898.7$ MeV at different times on the reaction plane for $\ell = 100\hbar$.

results of TDHF calculations for different values of initial orbital angular momentum ℓ_i are recorded as final values of mass and charge numbers of uranium-like A_1^f and Z_1^f and Curium-like A_2^f and Z_2^f fragments, final total kinetic energy (TKE), and scattering angles in the center of mass frame (c.m.) for four different collision geometries. Quantal diffusion coefficients are determined in terms of only occupied single-particle wave functions of TDHF. As an example, Fig. 2 shows the neutron and proton diffusion coefficients of $^{238}\text{U} + ^{248}\text{Cm}$ system at $E_{c.m.} = 898.7$ MeV for the initial angular momentum $\ell = 100\hbar$.

After colliding nuclei form a dinuclear system, the nucleon drift mechanism is determined via the potential energy surface in the (N, Z) plane. The drift paths of U-like fragments for each of the four distinct geometries are plotted for the $^{238}\text{U} + ^{248}\text{Cm}$ system in Fig. 3 for initial angular momentum $\ell = 100\hbar$. In four geometries, that we consider, the di-nuclear system drifts along the isoscalar path toward a local equilibrium state. For collisions of actinide nuclei, the lighter local equilibrium state is located in the vicinity of the lead valley with neutron and proton numbers around $N_0 = 130$, $Z_0 = 82$, and the heavier local equilibrium state is located in the vicinity of the superheavy valley with neutron and proton numbers

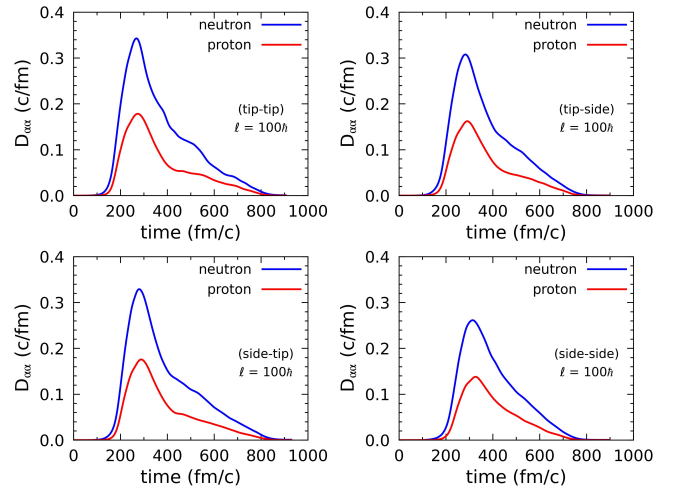


FIG. 2. Neutron and proton quantal diffusion coefficient in the $^{238}\text{U} + ^{248}\text{Cm}$ system at $E_{c.m.} = 898.7$ MeV in tip-tip, tip-side, side-tip, and side-side geometries for initial angular momentum $\ell = 100\hbar$.

around $N_0 = N_T - N_0 = 170$, $Z_0 = Z_T - Z_0 = 106$. In this system, the initial charge asymmetries $((N-Z)/(N+Z))$ of ^{238}U is 0.23 and that of ^{248}Cm is 0.23. These nuclei are located on the iso-scalar path with a charge asymmetry of 0.23. As illustrated in Fig. 3, the di-nuclear system formed in the collision of $^{238}\text{U} + ^{248}\text{Cm}$, U drifts nearly along the iso-scalar path, which is parallel to the equilibrium valley of stable nuclei. Drift paths contain additional specific details regarding the nucleon transfer mechanism by illustrating the system's evolution in the $N - Z$ plane. The isoscalar path produces an approximately $\phi = 31^\circ$ angle with the horizontal neutron axis as it extends completely toward the lead valley on one end and the superheavy valley on the other. In the $^{238}\text{U} + ^{248}\text{Cm}$ sys-

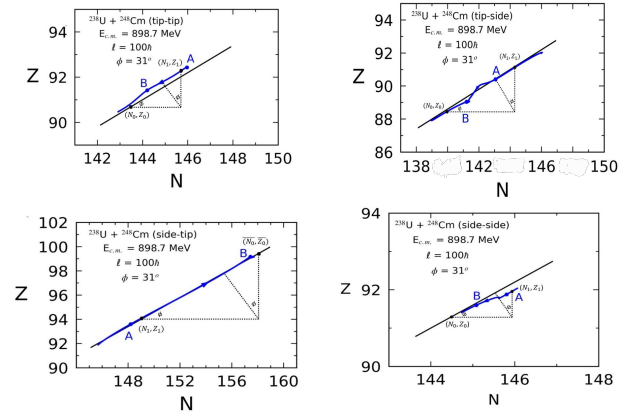


FIG. 3. Mean drift path in $N - Z$ plane for the projectile-like fragments in $^{238}\text{U} + ^{248}\text{Cm}$ the system at $E_{c.m.} = 898.7$ MeV in tip-tip, tip-side, side-tip, and side-side geometries. Solid blue lines denote the mean drift path of U-like fragments, and solid black lines denote the iso-scalar line.

tem, mean values of neutron and proton numbers of projectile-like fragments as a function of time are shown in Fig. 4 for the

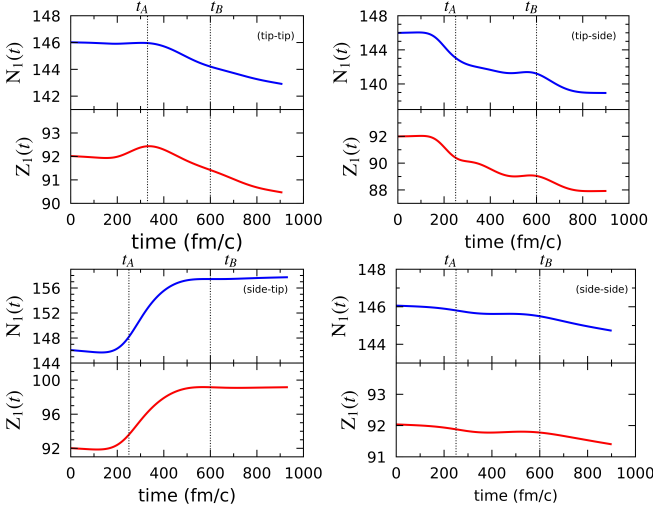


FIG. 4. Mean values of neutron and proton numbers of U-like fragments in the collision of the $^{238}\text{U} + ^{248}\text{Cm}$ system at $E_{c.m.} = 898.7$ MeV in tip-tip, tip-side, side-tip, and side-side collision geometries.

initial angular momentum $\ell = 100\hbar$. The labels A and B given in Fig. 3 and Fig. 4 indicate the projection of the time intervals used to determine the isoscalar curvature parameters.

The iso-scalar curvature parameter β is calculated by selecting the time intervals t_A and t_B shown in the graph of the average values of the neutron and proton numbers in Fig. 4, which correspond to the points A and B on the iso-scalar path given in Fig. 3, and the results are given in Table I.

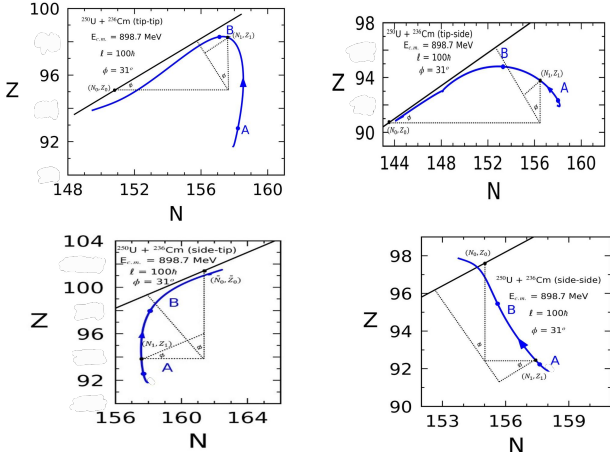


FIG. 5. Mean drift path in N-Z plane for the projectile-like fragments in $^{250}\text{U} + ^{236}\text{Cm}$ the system at $E_{c.m.} = 898.7$ MeV in tip-tip, tip-side, side-tip, and side-side geometries. Solid blue curves denote the mean drift path and black lines denote the iso-scalar line of U-like fragments. The labels A and B indicate the projection of the time intervals used to determine the isovector curvature parameters.

To extract information about potential energy in a perpendicular direction to the stability valley, we need to choose a reaction of a suitable system. For this purpose, the collision of a neighbor $^{250}\text{U} + ^{236}\text{Cm}$ system provides such a system.

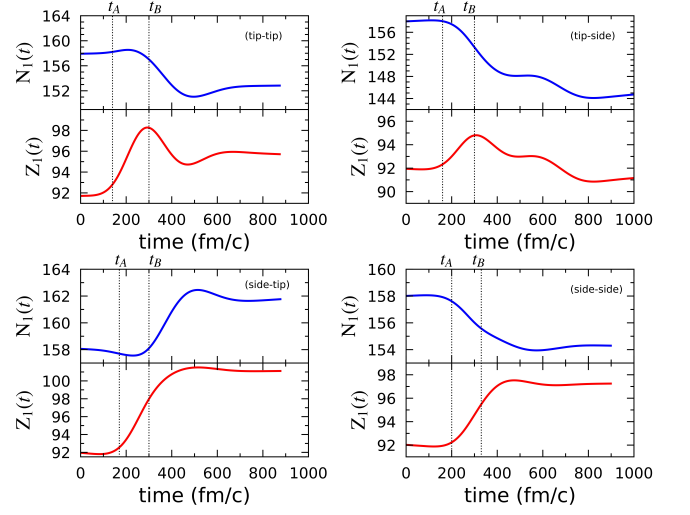


FIG. 6. Mean values of neutron and proton numbers of U-like fragments in the collision of the $^{250}\text{U} + ^{236}\text{Cm}$ system at $E_{c.m.} = 898.7$ MeV in tip-tip, tip-side, side-tip and side-side collision geometries.

Figure 5 shows the drift path of U-like fragments in the collision of $^{250}\text{U} + ^{236}\text{Cm}$ reaction at tip-tip, tip-side, side-tip, and side-side geometries at $E_{c.m.} = 898.7$ MeV. The perpendicular component of this drift line is referred to as the iso-vector path. Then, the system continues to drift along the iso-scalar path toward symmetry or asymmetry with the same charge asymmetry and the same slope angle as the iso-scalar path in the $^{238}\text{U} + ^{248}\text{Cm}$ system. Before the system reaches local equilibrium, it separates. By merging the drift data of these two very comparable systems, we can offer a rough description of the di-nuclear system's potential energy surface concerning the equilibrium value. In the $^{250}\text{U} + ^{236}\text{Cm}$ system, mean values of neutron and proton numbers of projectile-like fragments as a function of time are shown in Fig. 6 for initial angular momentum $\ell = 100\hbar$. The labels A and B given in Fig. 5 and Fig. 6 indicate the projection of the time intervals used to determine the isovector curvature parameters.

When the system drifts toward symmetry on the drift paths, the isoscalar distance from the local equilibrium state (N_0, Z_0) becomes $R_v(t) = (N_1 - N_0)\cos\phi + (Z_1 - Z_0)\sin\phi$ and the isovector distance from the isoscalar path as $R_s(t) = (Z_1 - Z_0)\cos\phi - (N_1 - N_0)\sin\phi$. When drift occurs toward asymmetry, the isoscalar distance from a local equilibrium state (\bar{N}_0, \bar{Z}_0) becomes $R_v(t) = (\bar{N}_0 - N_1)\cos\phi + (\bar{Z}_0 - Z_1)\sin\phi$ and the isovector distance as $R_s(t) = (\bar{N}_0 - N_1)\sin\phi - (\bar{Z}_0 - Z_1)\cos\phi$. The average values of the reduced curvature parameters are determined by

$$\alpha = \frac{1}{t_B - t_A} \int_{t_A}^{t_B} \left(\frac{v_n(\tau) \sin\phi}{D_{NN}(\tau)} - \frac{v_p(\tau) \cos\phi}{D_{ZZ}(\tau)} \right) \frac{1}{R_s} d\tau \quad (14)$$

$$\beta = \frac{1}{t_A - t_B} \int_{t_A}^{t_B} \left(\frac{v_n(\tau) \cos\phi}{D_{NN}(\tau)} + \frac{v_p(\tau) \sin\phi}{D_{ZZ}(\tau)} \right) \frac{1}{R_v} d\tau. \quad (15)$$

Transport coefficients are time-dependent because of the microscopic shell structure; hence, reduced curvature param-

eters are also time-dependent. We utilize constant curvature parameters and ignore the time dependency in the simple parabolic parametrization of the potential energy surface. The iso-vector curvature parameter α is calculated by selecting the time intervals t_A and t_B in the graph of the average values of the neutron and proton numbers shown in Fig. 6, which correspond to the points A and B on the iso-vector path given in Fig. 5, as well as the results given in Table I.

TABLE I. The calculated curvature parameters for $^{238}\text{U} + ^{248}\text{Cm}$ and $^{250}\text{U} + ^{236}\text{Cm}$ systems.

Orientation	$^{238}\text{U} + ^{248}\text{Cm}$				$^{250}\text{U} + ^{236}\text{Cm}$			
	XX	XY	YX	YY	XX	XY	YX	YY
t_A (fm/c)	330	250	250	250	140	160	170	250
t_B (fm/c)	600	600	600	750	300	300	300	350
β	0.004	0.004	0.010	0.004				
α					0.177	0.108	0.177	0.120

Variances and covariances are determined from the solutions of the coupled differential equations given in Eqs. (4,5,6) with initial conditions $\sigma_{NN}^2(t=0) = 0$, $\sigma_{ZZ}^2(t=0) = 0$, and $\sigma_{NZ}^2(t=0) = 0$, for each orbital angular momentum. As an example, Fig. 7 shows neutron, proton, and mixed variances, as a function of time, in the collision of $^{238}\text{U} + ^{248}\text{Cm}$ system at $E_{c.m.} = 898.7$ MeV for the tip-tip, tip-side, side-tip, and side-side collision geometries for $\ell = 100\hbar$. In the initial phase of the reaction, up to about $t = 300$ fm/c, we see that the magnitudes of the variances are in the order $\sigma_{NZ} < \sigma_{ZZ} < \sigma_{NN}$. The correlation develops over time and the order changes to $\sigma_{ZZ} < \sigma_{NZ} < \sigma_{NN}$. This shows the importance of correlations after significant energy dissipation. The neutron-proton σ_{NZ} correlation is zero in standard mean-field theories, and the effect of fluctuations does not agree with the observation in dissipative systems. In the stochastic mean-field approach, the σ_{NZ} correlation is not zero, and the effect of fluctuations agrees with the observation.

We present the numerical results of TDHF and SMF calculations for $^{238}\text{U} + ^{248}\text{Cm}$ reaction at $E_{c.m.} = 898.7$ MeV in Table II and Table III. The tables include asymptotic values of neutron dispersion $\sigma_{NN}(\ell)$, proton dispersion $\sigma_{ZZ}(\ell)$, mixed dispersions $\sigma_{NZ}(\ell)$, for each orbital angular momentum. The initial orbital angular momentum has been selected in increments of $20\hbar$ and then $40\hbar$. The TDHF code [62,63] was used in the computations using the SLy4d Skyrme energy density functional [64], with a box size of $60 \times 60 \times 36$ fm in the x-y-z directions, respectively.

In calculations, we perform a summation in the range from $\ell_{min} = 0\hbar$ to $\ell_{max} = 600\hbar$. We calculate total double cross-sections for tip-tip, tip-side, side-tip, and side-side geometries. Fig. 8 shows double cross-sections in ($N - Z$) plane for the production of primary fragments in tip-tip (a), tip-side (b), side-tip (c), and side-side (d) geometries. Large values of mixed variances indicate strong correlations in neutron-proton transfers. As a result, the major axes of equal cross-section elliptic curves are aligned along the valley of stability. The total cross-section calculations of secondary fragments are given in Fig. 9, assuming equal weights for contributions from each

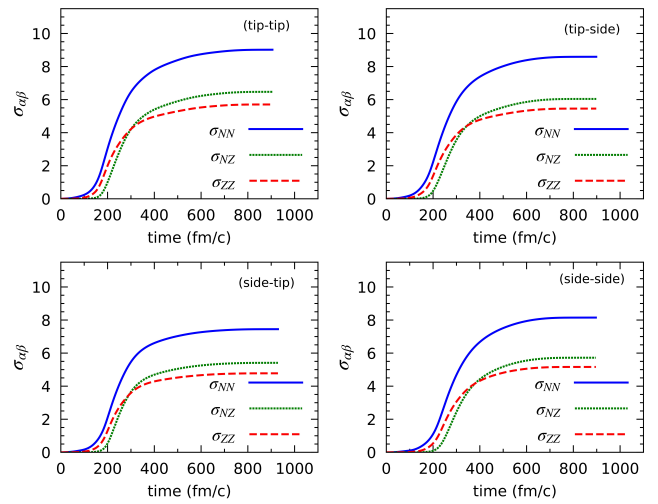


FIG. 7. Neutron, proton, and mixed variances as a function of time in the $^{238}\text{U} + ^{248}\text{Cm}$, $\ell = 100\hbar$. The system at $E_{c.m.} = 898.7$ MeV in tip-tip, tip-side, side-tip, and side-side collision geometries.

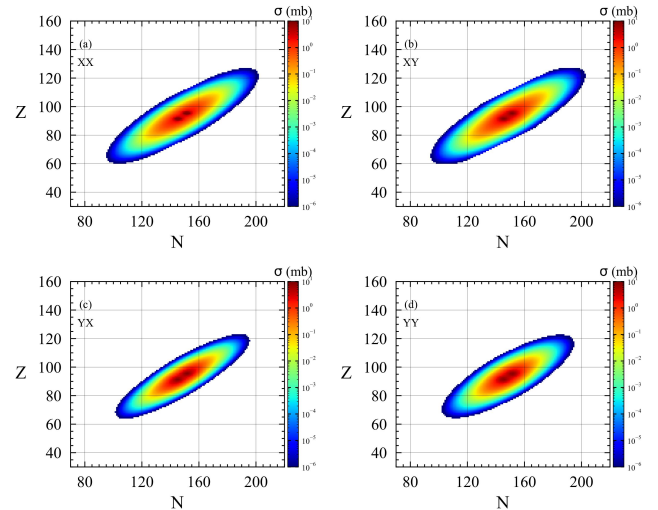


FIG. 8. Primary production cross sections in the $N - Z$ plane for the $^{238}\text{U} + ^{248}\text{Cm}$ system at $E_{c.m.} = 898.7$ MeV in tip-tip (XX), tip-side (XY), side-tip (YX), and side-side (YY) geometries

initial geometry. The comparison of the calculated critical values with the experimental values is given in Table. III. As the number of transferred nucleons increases, the cross-section decreases. The SMF results are consistent with the experimental values in terms of magnitude and peak points. The SMF results were successful in explaining the isotope cross-sections measured in the experiment.

The production of isotopes in the projectile-target combinations has been predicted theoretically. The results are obtained by using the quantal diffusion approach based on the SMF for primary production and secondary calculations by employing the GEMINI++ code. In Fig. 10, the calculated cross-sections for the transfer channels (+2p; Cf), (+3p; Es), (+4p; Fm), (+5p; Md) for the reaction $^{238}\text{U} + ^{248}\text{Cm}$ are compared with

TABLE II. Results of the TDHF and SMF calculations for the $^{238}\text{U} + ^{248}\text{Cm}$ system at $E_{c.m.} = 898.7$ MeV in tip-tip (XX), tip-side (XY) geometries.

-	ℓ_i (\hbar)	Z_1^f	A_1^f	Z_2^f	A_2^f	TKE	σ_{NN}	σ_{ZZ}	σ_{NZ}
XX	0	93.3	240.8	94.7	245.2	651.6	8.7	5.5	6.2
	20	93.2	240.5	94.8	245.2	623.9	8.8	5.5	6.2
	40	92.7	239.4	95.2	246.6	628.4	8.8	5.5	6.2
	60	92.1	237.5	95.9	248.5	630.9	8.8	5.5	6.3
	80	91.3	235.5	96.6	250.4	619.5	8.9	5.6	6.3
	100	90.6	233.6	97.4	252.4	592.9	9.0	5.7	6.5
	120	90.2	232.4	97.8	253.6	565.7	9.1	5.7	6.5
	140	90.4	233.3	97.6	252.7	545.0	9.2	5.8	6.6
	160	90.4	233.3	97.6	252.7	536.8	9.2	5.8	6.6
	180	90.2	232.5	97.8	253.5	543.4	9.1	5.8	6.6
	200	90.7	234.0	97.3	252.0	557.9	9.1	5.7	6.5
	240	91.8	236.9	96.1	249.1	573.1	8.9	5.6	6.3
	280	92.5	238.5	95.5	247.5	592.7	8.5	5.4	6.0
	320	92.4	237.8	95.6	248.2	637.5	8.0	5.0	5.5
	360	92.0	237.1	96.0	257.1	687.0	7.1	4.5	4.8
	400	91.2	235.3	96.8	250.7	737.1	6.0	3.8	3.7
	440	91.5	236.3	96.5	249.7	806.7	4.5	2.8	2.1
	480	91.9	237.7	96.1	248.3	876.6	2.5	1.3	0.5
	520	92.0	237.9	96.0	248.1	889.4	1.6	0.8	0.2
	560	92.0	238.0	96.0	248.0	891.1	1.2	0.5	0.1
600	92.0	238.0	96.0	248.0	892.1	1.1	0.4	0.1	
XY	0	86.9	223.6	101.1	262.4	653.9	8.5	5.4	6.0
	20	86.9	223.8	101.0	262.2	655.4	8.5	5.4	6.0
	40	87.1	224.3	101.0	261.7	654.2	8.5	5.4	6.0
	60	87.3	225.0	100.7	261.0	651.6	8.5	5.4	6.0
	80	87.6	225.4	100.4	260.2	646.2	8.5	5.4	5.9
	100	87.9	226.6	100.1	259.4	638.7	8.6	5.5	6.0
	120	88.2	227.6	99.7	258.4	626.0	8.6	5.5	6.1
	140	88.5	228.5	99.5	257.5	611.3	8.6	5.5	6.1
	160	89.0	229.7	99.0	256.3	598.0	8.7	5.5	6.1
	180	89.7	231.6	98.3	254.4	588.8	8.6	5.5	6.1
	200	90.6	234.2	97.4	251.8	585.8	8.6	5.4	6.2
	240	91.8	237.5	96.2	248.5	602.5	8.4	5.3	5.8
	280	91.5	236.0	96.5	250.0	620.5	8.1	5.2	5.6
	320	91.9	237.0	96.1	249.0	646.4	7.7	4.9	5.2
	360	92.7	239.0	95.3	284.7	674.4	7.2	4.6	4.8
	400	92.9	239.4	95.0	246.6	703.2	6.5	4.2	4.2
	440	93.0	239.6	95.0	246.4	740.3	5.8	3.7	3.4
	480	92.9	239.6	95.1	246.4	782.9	4.9	3.1	2.4
	520	92.5	238.9	95.5	247.0	829.0	3.8	2.3	1.4
	560	92.1	238.2	95.9	247.8	870.9	2.3	1.2	0.4
600	92.0	238.0	96.0	248.0	886.6	1.6	0.8	0.2	

TABLE III. Results of the TDHF and SMF calculations for the $^{238}\text{U} + ^{248}\text{Cm}$ system at $E_{c.m.} = 898.7$ MeV in side-tip (YX) and side-side (YY) geometries.

-	ℓ_i (\hbar)	Z_1^f	A_1^f	Z_2^f	A_2^f	TKE	σ_{NN}	σ_{ZZ}	σ_{NZ}
YX	0	88.0	226.3	100.0	259.6	627.7	7.3	4.7	5.3
	20	88.0	226.3	100.0	259.6	627.9	7.3	4.7	5.3
	40	87.9	226.2	100.0	259.8	625.3	7.4	4.7	5.3
	60	87.9	226.5	100.0	259.4	620.4	7.4	4.7	5.3
	80	88.1	227.3	99.9	258.7	610.3	7.4	4.8	5.4
	100	88.9	229.2	99.1	256.8	594.5	7.5	4.8	5.4
	120	90.2	232.9	97.8	253.1	582.4	7.5	4.8	5.4
	140	91.6	236.9	96.4	249.1	581.6	7.5	4.8	5.4
	160	92.4	239.2	95.6	246.8	588.0	7.5	4.8	5.4
	180	92.9	240.7	95.1	245.3	595.3	7.4	4.8	5.4
	200	93.3	241.8	94.7	244.2	604.3	7.4	4.7	5.3
	240	93.5	241.8	94.5	244.2	611.8	7.2	4.6	5.2
	280	93.8	242.8	94.2	243.2	615.1	7.0	4.5	5.1
	320	92.7	240.0	95.3	246.0	642.4	6.7	4.3	4.8
	360	92.2	238.4	95.8	247.6	680.9	6.3	4.1	4.4
	400	91.8	237.3	96.2	248.7	715.7	5.8	3.7	4.0
	440	91.3	236.0	96.7	249.9	749.2	5.2	3.4	3.3
	480	91.2	235.6	96.8	250.4	783.6	4.4	2.9	2.6
	520	91.3	235.9	96.7	250.0	824.2	3.6	2.3	1.7
	560	91.6	236.8	96.4	249.2	857.4	2.7	1.6	0.9
600	91.9	237.7	96.1	248.0	882.3	1.7	0.8	0.3	
YY	0	91.6	236.3	96.4	249.6	667.5	8.1	5.1	5.7
	20	91.6	236.4	96.3	249.6	668.7	8.1	5.1	5.7
	40	91.6	236.5	96.4	249.5	668.5	8.1	5.2	5.7
	60	91.6	236.6	96.4	249.4	668.6	8.2	5.2	5.7
	80	91.6	236.6	96.4	249.4	666.2	8.2	5.2	5.7
	100	90.6	233.6	97.4	252.4	665.3	8.2	5.2	5.7
	120	90.2	236.4	96.6	249.6	660.7	8.1	5.2	5.7
	140	91.5	236.6	96.5	249.4	656.7	8.1	5.1	5.7
	160	91.7	237.1	96.3	248.9	653.7	8.1	5.1	5.6
	180	92.1	237.9	95.9	248.1	650.3	8.0	5.1	5.6
	200	92.5	238.9	95.5	247.1	648.9	7.9	5.0	5.5
	240	93.0	240.3	95.0	245.7	651.2	7.7	4.9	5.3
	280	92.7	239.9	95.5	246.1	661.6	7.3	4.7	4.9
	320	92.6	239.5	95.4	246.5	670.0	6.9	4.4	4.6
	360	95.5	239.1	95.5	246.9	691.0	6.4	4.1	4.1
	400	92.3	238.6	95.7	247.4	734.9	5.8	3.7	3.5
	440	92.2	238.1	95.8	247.9	772.7	5.1	3.2	2.8
	480	92.1	237.7	95.9	248.3	810.7	4.2	2.6	1.9
	520	91.9	237.5	96.1	248.5	846.1	3.8	1.9	1.1
	560	91.9	237.6	96.1	248.4	871.9	2.5	1.3	0.5
600	92.0	237.8	96.0	248.2	882.7	1.9	1.0	0.3	

the experimental data from reference [43]. For $Z = 98$ (Californium), the primary total data shows a peak cross-section of 10.4 mb, corresponding to a mass number of 251. This indicates that, during the initial stages of the reaction, fragment

production is most likely around this mass number, suggesting a preferred nucleon exchange and fragmentation pathway for Californium isotopes. In contrast, the secondary total data for $Z = 98$ reveals a lower cross-section value of 0.60 mb, associated with a mass number of 250, reflecting the redistribution

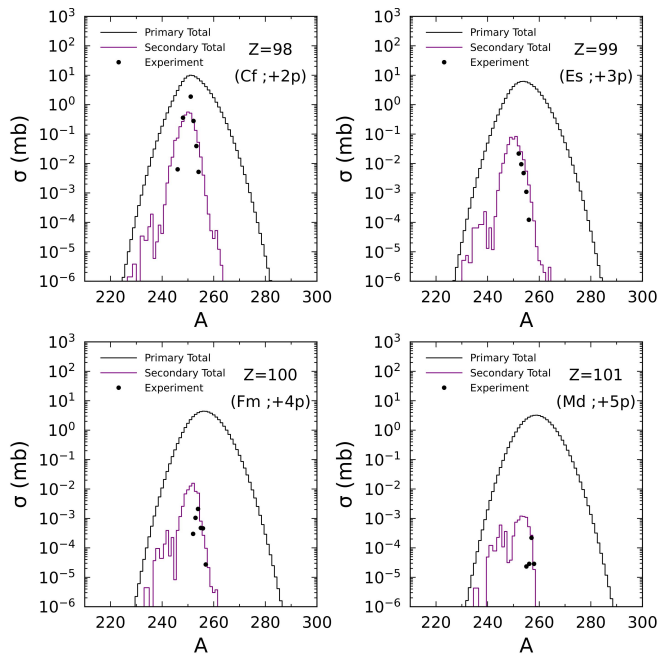


FIG. 9. Production cross sections of transuranium isotopes in the $^{238}\text{U} + ^{248}\text{Cm}$ system at $E_{c.m.} = 898.7$ MeV in tip-tip, tip-side, side-tip, and side-side collision geometries.

TABLE IV. Isotope Peak Points and Measured Values

Z	Primary Isotope		Secondary Isotope		Measured Values	
	Peak, A	σ (mb)	Peak, A	σ (mb)	Peak, A	σ (mb)
98	251	10.4	250	0.60	251	1.87
99	253	6.20	251	0.08	252	0.02
100	256	4.40	252	0.02	254	0.002
101	259	3.20	253	0.001	257	0.0002

of nucleons and energy during the de-excitation process. For $Z = 99$ (Einsteinium), the primary total data indicates a mass number of 253 with a corresponding cross-section of 6.20 mb, suggesting a significant likelihood of fragment production for this mass number during the initial reaction stages. For the secondary total data indicates a mass number of 251 with a corresponding cross section of 0.08 mb. Turning to $Z = 100$ (Fermium), the primary total data reveals a mass number of 256 with a cross-section of 4.40 mb, indicating a notable probability for fragment production in this region. The secondary total data for $Z = 100$, however, shows a mass number of 252 and a significantly lower cross-section of 0.02 mb, highlighting a decrease in fragment production likelihood during the secondary stages. For $Z = 101$ (Mendelevium), the primary total data reflects a mass number of 259 with a cross-section of 3.20 mb, suggesting a consistent fragmentation pathway in the initial reaction. Conversely, the secondary total data for $Z=101$ shows a mass number of 253 with a minimal cross-section of 0.001 mb, emphasizing a marked reduction in the probability of fragment production in this mass range during the later stages. These findings underscore the complex behavior of Californium, Einsteinium, Fermium, and Mendelevium

during nuclear reactions, with distinct mass distributions evolving from the primary to secondary stages of fragmentation. The data illustrate how variations in Z influences the outcomes of nuclear reactions modeled by SMF+GEMINI. It is observed that the calculated results align closely with the experimental data, indicating the reliability of the theoretical models used in this analysis. This agreement is particularly evident in the behavior of the cross sections, which exhibit a rapid decrease as the mass number of the produced fragments increases. As the atomic number of the surviving heavy nuclei rises, the cross sections shift toward regions of higher mass numbers. This trend suggests that the increasing stability and interaction characteristics of heavier nuclei play a significant role in fragment production.

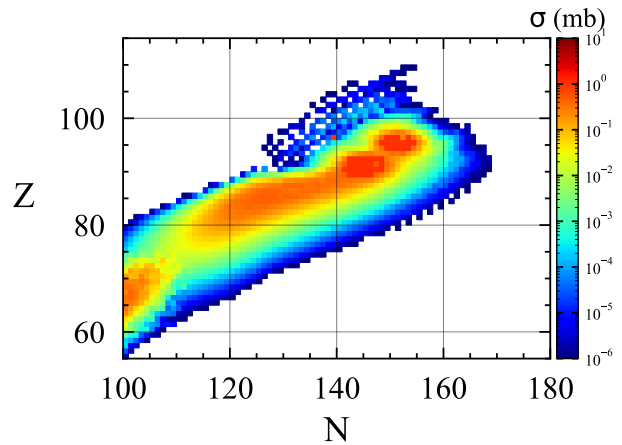


FIG. 10. Calculated total production cross sections of secondary isotopes in the $(N-Z)$ plane for the $^{238}\text{U} + ^{248}\text{Cm}$ system at $E_{c.m.} = 898.7$ MeV energy

The calculated total production cross-sections of secondary isotopes in the $(N-Z)$ plane for the transuranium and superheavy regions for the $^{238}\text{U} + ^{248}\text{Cm}$ system at $E_{c.m.} = 898.7$ MeV energy are given in Fig. 10. The isotope production cross sections can be obtained in the millibarn range for the $Z=93-98$ region, in the microbarn range in the $Z = 99 - 102$ region, and in the nanobarn range for the $Z = 103 - 110$ region. It was shown that the $^{238}\text{U} + ^{248}\text{Cm}$ system at $E_{c.m.} = 898.7$ MeV energy is a suitable system for the synthesis of transuranium neutron-rich superheavy isotopes.

In low-energy collisions, the cross-section is very sensitive to shell effects. During the de-excitation processes in the MNT reaction, the cross-section values decrease due to strong shell effects. In this case, the expected magic number isotopes ($Z=114, N=184$) in the island of stability, in the superheavy region, could not be reached. Theoretical results calculated for the $Z = 102 - 105$ region, for which there are no experimental data, are given in Fig. 11, and it was found that the cross-section values would be smaller than the microbarn level.

The decay processes of MNT products are related to the

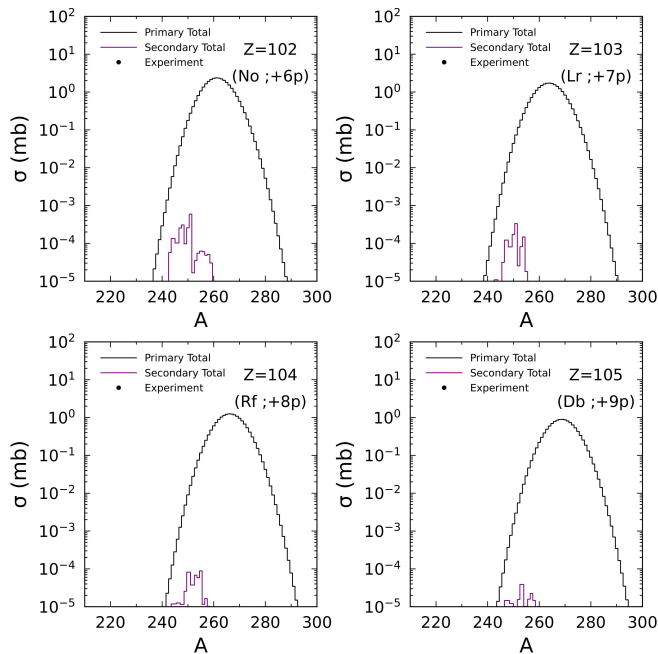


FIG. 11. SMF+GEMINI++ calculations of total production cross-sections of $Z = 102 - 105$ isotopes in the $^{238}\text{U} + ^{248}\text{Cm}$ $E_{c.m.} = 898.7$ reaction

local excitation energy and angular momentum at the equilibrium time, fission barrier, and separation energy of evaporated particles (neutron, proton, deuterium, triton, alpha, etc.). A strong shell effect can increase the fission barrier and separation energy, which ensures the survival of the primary fragment. Shell effect can increase MNT yields by up to two orders of magnitude. In the absence of shell effect, the production cross sections of primary and secondary fragments decrease monotonically with mass or charge number, which reduces the formation of heavy rare isotopes in MNT reactions.

IV. CONCLUSIONS

In this study, we present an investigation of the multinucleon transfer mechanism in collisions of $^{238}\text{U} + ^{248}\text{Cm}$ sys-

tem at $E_{c.m.} = 898.7$ MeV employing a quantal diffusion description, which provides a source for developing fluctuations, based on the SMF approach beyond the TDHF theory. The standard mean-field description of TDHF determines the average evolution of the most probable path of heavy-ion collision dynamics, however, the SMF provides an extension of the standard TDHF description by including mean-field fluctuations consistent with the fluctuation-dissipation theorem of non-equilibrium statistical mechanics. Transport coefficients include quantal effects due to shell structure and Pauli blocking, and do not involve any adjustable parameters other than the standard parameters of the effective Skyrme force used in TDHF description.

Highly excited primary fragments decay by particle emission and secondary fission. The de-excitation processes of primary fragments are followed with statistical code GEMINI++ and the production cross-sections of the secondary fragments are calculated. The observed agreement between the calculated and experimental data shows that the SMF approach is a powerful way to explain the MNT process. The SMF approach is an effective microscopic and quantal approach for the synthesis of neutron-rich isotopes farther from the target or superheavy elements by MNT reactions.

V. ACKNOWLEDGEMENTS

S.A. gratefully acknowledges Middle East Technical University for the warm hospitality extended to him during his visits. This work is supported in part by US DOE Grants No. DE-SC0013847. This work is supported in part by TUBITAK Grant No. 122F150. The numerical calculations reported in this paper were partially performed at TUBITAK ULAKBIM, High Performance and Grid Computing Center (TRUBA resources).

-
- [1] G. G. Adamian, N. V. Antonenko, A. Diaz-Torres, and S. Heinz, How to extend the chart of nuclides?, *Eur. Phys. J. A* **56**, 47 (2020).
 - [2] G. Münzenberg, M. Gupta, H. M. Devaraja, Y. K. Gambhir, S. Heinz, and S. Hofmann, Heavy and superheavy elements: next generation experiments, ideas and considerations, *Eur. Phys. J. A* **59**, 21 (2023).
 - [3] T. Niwase, Y. X. Watanabe, Y. Hirayama, M. Mukai, P. Schury, A. N. Andreyev, T. Hashimoto, S. Iimura, H. Ishiyama, Y. Ito, S. C. Jeong, D. Kaji, S. Kimura, H. Miyatake, K. Morimoto, J.-Y. Moon, M. Oyaizu, M. Rosenbusch, A. Taniguchi, and M. Wada, Discovery of New Isotope ^{241}U and Systematic High-Precision Atomic Mass Measurements of Neutron-Rich Pa-Pu Nuclei Produced via Multinucleon Transfer Reactions, *Phys. Rev. Lett.* **130**, 132502 (2023).
 - [4] Valery Zagrebaev and Walter Greiner, New way for the production of heavy neutron-rich nuclei, *J. Phys. G: Nucl. Part. Phys.* **35**, 125103 (2008).
 - [5] Valery Zagrebaev and Walter Greiner, Production of New Heavy Isotopes in Low-Energy Multinucleon Transfer Reactions, *Phys. Rev. Lett.* **101**, 122701 (2008).
 - [6] V. I. Zagrebaev and W. Greiner, Production of heavy and superheavy neutron-rich nuclei in transfer reactions, *Phys. Rev. C* **83**, 044618 (2011).

- [7] A. V. Karpov and V. V. Saiko, Modeling near-barrier collisions of heavy ions based on a Langevin-type approach, *Phys. Rev. C* **96**, 024618 (2017).
- [8] V. V. Saiko and A. V. Karpov, Analysis of multinucleon transfer reactions with spherical and statically deformed nuclei using a Langevin-type approach, *Phys. Rev. C* **99**, 014613 (2019).
- [9] V. Saiko and A. Karpov, Multinucleon transfer as a method for production of new heavy neutron-enriched isotopes of transuranium elements, *Eur. Phys. J. A* **58**, 41 (2022).
- [10] Z.-Q. Feng, G.-M. Jin, and J.-Q. Li, Production of heavy isotopes in transfer reactions by collisions of $^{238}\text{U} + ^{238}\text{U}$, *Phys. Rev. C* **80**, 067601 (2009).
- [11] Z.-Q. Feng, Production of neutron-rich isotopes around $N = 126$ in multinucleon transfer reactions, *Phys. Rev. C* **95**, 024615 (2017).
- [12] K. Zhao, X. Wu, and Z. Li, Quantum molecular dynamics study of the mass distribution of products in 7.0A MeV $^{238}\text{U} + ^{238}\text{U}$ collisions, *Phys. Rev. C* **80**, 054607 (2009).
- [13] K. Zhao, Z. Li, Y. Zhang, N. Wang, Q. Li, C. Shen, Y. Wang, and X. Wu, Production of unknown neutron-rich isotopes in $^{238}\text{U} + ^{238}\text{U}$ collisions at near-barrier energy, *Phys. Rev. C* **94**, 024601 (2016).
- [14] N. Wang and L. Guo, New neutron-rich isotope production in $^{154}\text{Sm} + ^{160}\text{Gd}$, *Phys. Lett. B* **760**, 236 (2016).
- [15] C. Simenel, Nuclear quantum many-body dynamics, *Eur. Phys. J. A* **48**, 152 (2012).
- [16] C. Simenel and A. S. Umar, Heavy-ion collisions and fission dynamics with the time-dependent Hartree-Fock theory and its extensions, *Prog. Part. Nucl. Phys.* **103**, 19 (2018).
- [17] T. Nakatsukasa, K. Matsuyanagi, M. Matsuo, and K. Yabana, Time-dependent density-functional description of nuclear dynamics, *Rev. Mod. Phys.* **88**, 045004 (2016).
- [18] V. E. Oberacker, A. S. Umar, and C. Simenel, Dissipative dynamics in quasifission, *Phys. Rev. C* **90**, 054605 (2014).
- [19] A. S. Umar, V. E. Oberacker, and C. Simenel, Shape evolution and collective dynamics of quasifission in the time-dependent Hartree-Fock approach, *Phys. Rev. C* **92**, 024621 (2015).
- [20] A. S. Umar and V. E. Oberacker, Time-dependent HF approach to SHE dynamics, *Nucl. Phys. A* **944**, 238 (2015).
- [21] A. S. Umar, C. Simenel, and W. Ye, Transport properties of isospin asymmetric nuclear matter using the time-dependent Hartree-Fock method, *Phys. Rev. C* **96**, 024625 (2017).
- [22] C. Simenel, Particle Transfer Reactions with the Time-Dependent Hartree-Fock Theory Using a Particle Number Projection Technique, *Phys. Rev. Lett.* **105**, 192701 (2010).
- [23] K. Sekizawa and K. Yabana, Time-dependent Hartree-Fock calculations for multinucleon transfer and quasifission processes in the $^{64}\text{Ni} + ^{238}\text{U}$ reaction, *Phys. Rev. C* **93**, 054616 (2016).
- [24] K. Godbey, A. S. Umar, and C. Simenel, Deformed shell effects in $^{48}\text{Ca} + ^{249}\text{Bk}$ quasifission fragments, *Phys. Rev. C* **100**, 024610 (2019).
- [25] C. Simenel, K. Godbey, and A. S. Umar, Timescales of Quantum Equilibration, Dissipation and Fluctuation in Nuclear Collisions, *Phys. Rev. Lett.* **124**, 212504 (2020).
- [26] R. Balian and M. Vénéroni, Time-dependent variational principle for the expectation value of an observable: Mean-field applications, *Ann. Phys. (NY)* **164**, 334 (1985).
- [27] R. Balian and M. Vénéroni, Correlations and fluctuations in static and dynamic mean-field approaches, *Ann. Phys.* **216**, 351 (1992).
- [28] C. Simenel, Particle-Number Fluctuations and Correlations in Transfer Reactions Obtained Using the Balian-Vénéroni Variational Principle, *Phys. Rev. Lett.* **106**, 112502 (2011).
- [29] E. Williams, K. Sekizawa, D. J. Hinde, C. Simenel, M. Dasgupta, I. P. Carter, K. J. Cook, D. Y. Jeung, S. D. McNeil, C. S. Palshetkar, D. C. Rafferty, K. Ramachandran, and A. Wakhle, Exploring Zeptosecond Quantum Equilibration Dynamics: From Deep-Inelastic to Fusion-Fission Outcomes in $^{58}\text{Ni} + ^{60}\text{Ni}$ Reactions, *Phys. Rev. Lett.* **120**, 022501 (2018).
- [30] K. Godbey and A. S. Umar, Quasifission Dynamics in Microscopic Theories, *Front. Phys.* **8**, 40 (2020).
- [31] K. Godbey, C. Simenel, and A. S. Umar, Microscopic predictions for the production of neutron-rich nuclei in the reaction $^{176}\text{Yb} + ^{176}\text{Yb}$, *Phys. Rev. C* **101**, 034602 (2020).
- [32] S. Ayik, A stochastic mean-field approach for nuclear dynamics, *Phys. Lett. B* **658**, 174 (2008).
- [33] D. Lacroix and S. Ayik, Stochastic quantum dynamics beyond mean field, *Eur. Phys. J. A* **50**, 95 (2014).
- [34] S. Ayik, B. Yilmaz, O. Yilmaz, and A. S. Umar, Quantal diffusion description of multinucleon transfers in heavy-ion collisions, *Phys. Rev. C* **97**, 054618 (2018).
- [35] S. Ayik, B. Yilmaz, O. Yilmaz, and A. S. Umar, Quantal diffusion approach for multinucleon transfers in Xe + Pb collisions, *Phys. Rev. C* **100**, 014609 (2019).
- [36] K. Sekizawa and S. Ayik, Quantal diffusion approach for multinucleon transfer processes in the $^{58,64}\text{Ni} + ^{208}\text{Pb}$ reactions: Toward the production of unknown neutron-rich nuclei, *Phys. Rev. C* **102**, 014620 (2020).
- [37] O. Yilmaz, G. Turan, and B. Yilmaz, Quasi-fission and fusion-fission reactions in $^{48}\text{Ca} + ^{208}\text{Pb}$ collisions at $E_{\text{c.m.}} = 190$ MeV, *Eur. Phys. J. A* **56**, 37 (2020).
- [38] S. Ayik, B. Yilmaz, O. Yilmaz, and A. S. Umar, Merging of transport theory with the time-dependent Hartree-Fock approach: Multinucleon transfer in U + U collisions, *Phys. Rev. C* **102**, 024619 (2020).
- [39] S. Ayik, M. Arik, E. C. Karanfil, O. Yilmaz, B. Yilmaz, and A. S. Umar, Quantal diffusion description of isotope production via the multinucleon transfer mechanism in $^{48}\text{Ca} + ^{238}\text{U}$ collisions, *Phys. Rev. C* **104**, 054614 (2021).
- [40] S. Ayik, M. Arik, O. Yilmaz, B. Yilmaz, and A. S. Umar, Multinucleon transfer mechanism in $^{250}\text{Cf} + ^{232}\text{Th}$ collisions using the quantal transport description based on the stochastic mean-field approach, *Phys. Rev. C* **107**, 014609 (2023).
- [41] S. Ayik, M. Arik, E. Erbayri, O. Yilmaz, and A. S. Umar, Multinucleon transfer mechanism in $^{160}\text{Gd} + ^{186}\text{W}$ collisions in stochastic mean-field theory, *Phys. Rev. C* **108**, 054605 (2023).
- [42] Kayaalp, A., Ocal, S. E., Yaprakli, B., Arik, M., Ayik, S., Yilmaz, O., and Umar, A. S., A theoretical study on quasifission and fusion-fission processes in heavy-ion collisions, *Eur. Phys. J. A* **60**, 79 (2024).
- [43] J. V. Kratz, M. Schädel, and H. W. Gäggeler, Reexamining the heavy-ion reactions $^{238}\text{U} + ^{238}\text{U}$ and $^{238}\text{U} + ^{248}\text{Cm}$ and actinide production close to the barrier, *Phys. Rev. C* **88**, 054615 (2013).
- [44] M. Schädel, W. Brüche, H. Gäggeler, J. V. Kratz, K. Sümmerner, G. Wirth, G. Herrmann, R. Stakemann, G. Tittel, N. Trautmann, J. M. Nitschke, E. K. Hulet, R. W. Lougheed, R. L. Hahn, and R. L. Ferguson, Actinide Production in Collisions of ^{238}U with ^{248}Cm , *Phys. Rev. Lett.* **48**, 852 (1982).
- [45] J. V. Kratz, W. Loveland, and K. J. Moody, Syntheses of transuranium isotopes with atomic numbers $Z \leq 103$ in multinucleon transfer reactions, *Nucl. Phys. A* **944**, 117 (2015).
- [46] C. Peng and Z.-Q. Feng, Production of neutron-rich heavy nuclei around $N = 162$ in multinucleon transfer reactions, *Eur. Phys. J. A* **58**, 162 (2022).
- [47] T. L. Zhao, X. J. Bao, and H. F. Zhang, Exploring the optimal way to produce $Z=100$ -106 neutron-rich nuclei, *Phys. Rev. C* **108**, 024602 (2023).

- [48] Hannes Risken and Till Frank, *The Fokker–Planck Equation* (Springer–Verlag, Berlin, 1996).
- [49] W. U. Schröder, J. R. Huizenga, and J. Randrup, Correlated mass and charge transport induced by statistical nucleon exchange in damped nuclear reactions, *Phys. Lett. B* **98**, 355 (1981).
- [50] A. C. Merchant and W. Nörenberg, Neutron and proton diffusion in heavy-ion collisions, *Phys. Lett. B* **104**, 15 (1981).
- [51] C. W. Gardiner, *Quantum Noise* (Springer–Verlag, Berlin, 1991).
- [52] U. Weiss, *Quantum Dissipative Systems*, 2nd ed. (World Scientific, Singapore, 1999).
- [53] W. Nörenberg, Memory effects in the energy dissipation for slow collective nuclear motion, *Phys. Lett. B* **104**, 107 (1981).
- [54] J. Randrup, Theory of transfer-induced transport in nuclear collisions, *Nucl. Phys. A* **327**, 490 (1979).
- [55] A. C. Merchant and W. Nörenberg, Microscopic transport theory of heavy-ion collisions, *Z. Phys. A* **308**, 315 (1982).
- [56] R. Charity, *GEMINI: A code to simulate the decay of a compound nucleus by a series of binary decays*, Tech. Rep. (International Atomic Energy Agency (IAEA), 2008) INDC(NDS)–0530.
- [57] W. Hauser and H. Feshbach, The Inelastic Scattering of Neutrons, *Phys. Rev.* **87**, 366 (1952).
- [58] L. G. Moretto, Statistical emission of large fragments: A general theoretical approach, *Nucl. Phys. A* **247**, 211 (1975).
- [59] L. G. Moretto and G. J. Wozniak, The role of the compound nucleus in complex fragment emission at low and intermediate energies, *Prog. Part. Nucl. Phys.* **21**, 401 (1988).
- [60] J. M. Blatt and V. F. Weisskopf, *Theoretical Nuclear Physics* (Springer New York, NY, 1979).
- [61] David J. Kedziora and Cédric Simenel, New inverse quasifission mechanism to produce neutron-rich transfermium nuclei, *Phys. Rev. C* **81**, 044613 (2010).
- [62] A. S. Umar, M. R. Strayer, J. S. Wu, D. J. Dean, and M. C. Güçlü, Nuclear Hartree-Fock calculations with splines, *Phys. Rev. C* **44**, 2512 (1991).
- [63] A. S. Umar and V. E. Oberacker, Three-dimensional unrestricted time-dependent Hartree-Fock fusion calculations using the full Skyrme interaction, *Phys. Rev. C* **73**, 054607 (2006).
- [64] Ka-Hae Kim, Takaharu Otsuka, and Paul Bonche, Three-dimensional TDHF calculations for reactions of unstable nuclei, *J. Phys. G: Nucl. Part. Phys.* **23**, 1267 (1997).